

# Polarization sensitive, three-dimensional, single-molecule imaging of cells with a double-helix system

Sri Rama Prasanna Pavani<sup>1\*</sup>, Jennifer G. DeLuca<sup>2</sup>, and Rafael Piestun<sup>1</sup>

<sup>1</sup>Department of Electrical and Computer Engineering, University of Colorado, Boulder, CO 80309, USA

<sup>2</sup>Dept. of Biochemistry and Molecular Biology, Colorado State University, Fort Collins, CO 80523, USA

\*pavani@colorado.edu

**Abstract:** Double-helix point spread function photoactivation-localization microscopy allows three-dimensional (3D) superresolution imaging of objects smaller than the optical diffraction-limit. We demonstrate polarization sensitive detection with 3D super-localization of single-molecules and unveil 3D polarization specific characteristics of single-molecules within the intracellular structure of PtK1 cells expressing photoactivatable green fluorescent protein. The system modulates orthogonal polarization components of single-molecule emissions with a single spatial light modulator and detects them separately with a single detector. Information obtained from the two polarization channels demonstrates polarization based contrast in 3D superresolution imaging. Further, we show that the 3D information from the two channels can be optimally combined to yield up to 30% improvement in localization precision relative to a single polarization channel system.

©2009 Optical Society of America

**OCIS codes:** (260.5430) Polarization; (100.6640) Superresolution; (180.6900) Three-dimensional microscopy; (110.4850) Optical transfer functions; (180.2520) Fluorescence microscopy; (110.1758) Computational imaging.

---

## References and links

1. T. A. Klar, S. Jakobs, M. Dyba, A. Egner, and S. W. Hell, "Fluorescence microscopy with diffraction resolution barrier broken by stimulated emission," *Proc. Natl. Acad. Sci. U.S.A.* **97**(15), 8206–8210 (2000).
2. M. G. L. Gustafsson, "Surpassing the lateral resolution limit by a factor of two using structured illumination microscopy," *J. Microsc.* **198**(2), 82–87 (2000).
3. E. Betzig, G. H. Patterson, R. Sougrat, O. W. Lindwasser, S. Olenych, J. S. Bonifacino, M. W. Davidson, J. Lippincott-Schwartz, and H. F. Hess, "Imaging intracellular fluorescent proteins at nanometer resolution," *Science* **313**(5793), 1642–1645 (2006).
4. M. J. Rust, M. Bates, and X. Zhuang, "Sub-diffraction-limit imaging by stochastic optical reconstruction microscopy (STORM)," *Nat. Methods* **3**(10), 793–796 (2006).
5. S. T. Hess, T. P. K. Girirajan, and M. D. Mason, "Ultra-high resolution imaging by fluorescence photoactivation localization microscopy," *Biophys. J.* **91**(11), 4258–4272 (2006).
6. B. Huang, W. Wang, M. Bates, and X. Zhuang, "Three-dimensional super-resolution imaging by stochastic optical reconstruction microscopy," *Science* **319**(5864), 810–813 (2008).
7. M. F. Juetten, T. J. Gould, M. D. Lessard, M. J. Mlodzikowski, B. S. Nagpure, B. T. Bennett, S. T. Hess, and J. Bewersdorff, "Three-dimensional sub-100 nm resolution fluorescence microscopy of thick samples," *Nat. Methods* **5**(6), 527–529 (2008).
8. P. Prabhat, S. Ram, E. S. Ward, and R. J. Ober, "Simultaneous imaging of different focal planes in fluorescence microscopy for the study of cellular dynamics in three dimensions," *IEEE Trans. Nanobioscience* **3**(4), 237–242 (2004).
9. A. Vaziri, J. Tang, H. Shroff, and C. V. Shank, "Multilayer three-dimensional super resolution imaging of thick biological samples," *Proc. Natl. Acad. Sci. U.S.A.* **105**(51), 20221–20226 (2008).
10. G. Shtengel, J. A. Galbraith, C. G. Galbraith, J. Lippincott-Schwartz, J. M. Gillette, S. Manley, R. Sougrat, C. M. Waterman, P. Kanchanawong, M. W. Davidson, R. D. Fetter, and H. F. Hess, "Interferometric fluorescent super-resolution microscopy resolves 3D cellular ultrastructure," *Proc. Natl. Acad. Sci. U.S.A.* **106**(9), 3125–3130 (2009).
11. S. R. P. Pavani, M. A. Thompson, J. S. Biteen, S. J. Lord, N. Liu, R. J. Twieg, R. Piestun, and W. E. Moerner, "Three-dimensional, single-molecule fluorescence imaging beyond the diffraction limit by using a double-helix point spread function," *Proc. Natl. Acad. Sci. U.S.A.* **106**(9), 2995–2999 (2009).

12. S. R. P. Pavani, and R. Piestun, "High-efficiency rotating point spread functions," *Opt. Express* **16**(5), 3484–3489 (2008).
13. S. R. P. Pavani, and R. Piestun, "Three dimensional tracking of fluorescent microparticles using a photon-limited double-helix response system," *Opt. Express* **16**(26), 22048–22057 (2008).
14. S. R. P. Pavani, A. Greengard, and R. Piestun, "Three-dimensional localization with nanometer accuracy using a detector-limited double-helix point spread function system," *Appl. Phys. Lett.* **95**(2), 021103 (2009).
15. T. J. Gould, M. S. Gunewardene, M. V. Gudheti, V. V. Verkhusha, S.-R. Yin, J. A. Gosse, and S. T. Hess, "Nanoscale imaging of molecular positions and anisotropies," *Nat. Methods* **5**(12), 1027–1030 (2008).
16. T. Ha, T. Enderle, D. S. Chemla, and S. Weiss, "Single molecule dynamics studied by polarization modulation," *Phys. Rev. Lett.* **77**(19), 3979–3982 (1996).
17. R. M. Dickson, D. J. Norris, and W. E. Moerner, "Simultaneous Imaging of Individual Molecules Aligned Both Parallel and Perpendicular to the Optic Axis," *Phys. Rev. Lett.* **81**(24), 5322–5325 (1998).
18. B. Sick, B. Hecht, and L. Novotny, "Orientational imaging of single molecules by annular illumination," *Phys. Rev. Lett.* **85**(21), 4482–4485 (2000).
19. M. R. Foreman, C. M. Romero, and P. Török, "Determination of the three-dimensional orientation of single molecules," *Opt. Lett.* **33**(9), 1020–1022 (2008).
20. F. Aguet, S. Geissbühler, I. Märki, T. Lasser, and M. Unser, "Super-resolution orientation estimation and localization of fluorescent dipoles using 3-D steerable filters," *Opt. Express* **17**(8), 6829–6848 (2009).
21. G. H. Patterson, and J. Lippincott-Schwartz, "A photoactivatable GFP for selective photolabeling of proteins and cells," *Science* **297**(5588), 1873–1877 (2002).
22. A. Greengard, Y. Y. Schechner, and R. Piestun, "Depth from diffracted rotation," *Opt. Lett.* **31**(2), 181–183 (2006).
23. S. M. Kay, *Fundamentals of Statistical Signal Processing: Estimation Theory* (Prentice-Hall, 1993).
24. A. Yariv, and P. Yeh, *Photonics: Optical Electronics in Modern Communications* (Oxford University Press, New York, 2007).

## 1. Introduction

A variety of methods for superresolution optical microscopy are now making it possible to resolve objects that are smaller than the optical diffraction limit, which has historically restricted spatial resolution to about  $\sim 200\text{nm}$  in the transverse ( $x, y$ ) dimensions. Prominent among these are stimulated emission and depletion (STED) microscopy [1], structured illumination microscopy (SIM) [2], and photoactivated localization microscopy (PALM) / stochastic optical reconstruction microscopy (STORM) / Fluorescence photoactivation localization microscopy (FPALM) [3–5]. PALM, STORM, and FPALM essentially photoactivate (turn on) a sparse subset of fluorescent molecules at a given time, and localize the molecule positions with precision much better than the diffraction limit. Superresolution images are obtained by repeatedly photoactivating and localizing different sparse molecule subsets at different times, and by combining the position information of all photoactivated molecules. This has been extended to the third dimension by using astigmatism [6], biplane detection [7,8], two-photon processes [9], interferometry [10], and a double-helix point spread function (DH-PSF) [11].

The DH-PSF based 3D superresolution technique uses a phase mask [12] in a microscope's imaging path to engineer the point spread function of the microscope to exhibit two lobes that rotate with defocus. Accordingly, each molecule displays two lobes in the image plane, with the angular orientation of the lobes encoding the axial position of the molecule, and their midpoint representing the transverse position of the molecule. Because the DH-PSF carries higher Fisher Information about a molecule's 3D position than a standard (clear aperture) PSF over a long range, DH-PSF microscopes can localize molecules with fundamentally better 3D precision than standard systems [13,14].

In single-molecule superresolution imaging, it is useful to obtain information on the orientation of molecules by analyzing the polarization of their emissions, in addition to their spatial positions. Polarization sensitive superresolution imaging offers images with a molecule-orientation based contrast, besides the contrast based on the brightness and the concentration of single molecules. Polarization-FPALM demonstrates this capability in two dimensions by simultaneously detecting the transverse ( $x, y$ ) positions and polarization anisotropy of molecules [15]. Information on molecule orientations has also been obtained by other methods [16–20], but they have not been used in superresolution imaging.

In this paper, we present a polarization-sensitive DH-PSF superresolution system and demonstrate the first 3D nanoscale imaging of polarization-specific characteristics of single

photoactivatable green fluorescent protein (PA-GFP) [21] molecules in a cell. The system modulates the phase of two orthogonal polarization channels with a single spatial light modulator, and detects polarization-specific DH-PSF images with a single detector. Using a single objective lens, the 3D position of the molecules is estimated with about 20nm and 40nm precisions in the transverse and axial dimensions, with only ~250 detected photons per image. We further show that improved 3D localization precisions can be achieved by optimally combining the information from the two polarization channels.

## 2. Polarization sensitive 3D superresolution imaging

Figure 1 illustrates the polarization-sensitive 3D superresolution experimental setup. The imaging path includes a microscope section and a polarization sensitive signal processing section.

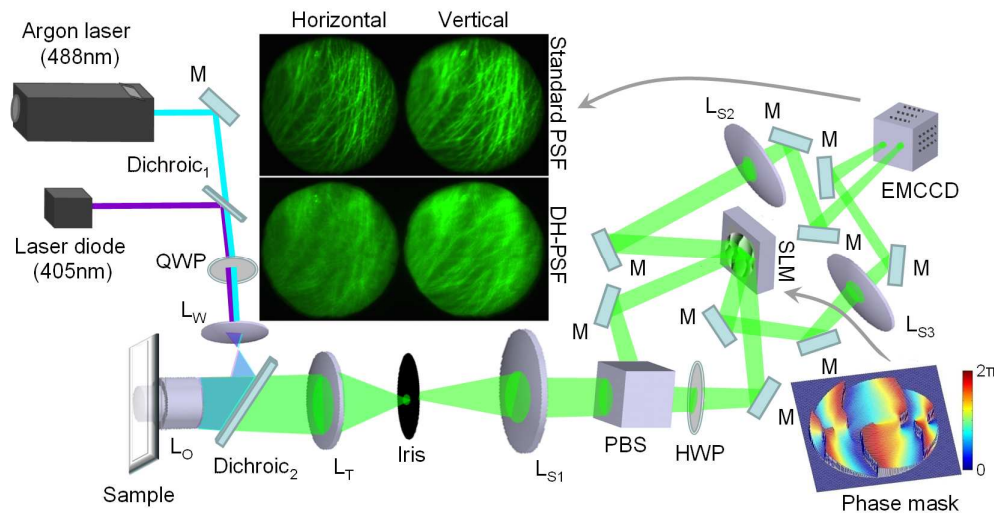


Fig. 1. Experimental setup for polarization sensitive 3D superresolution imaging with the double-helix point spread function (DH-PSF). PtK1 cells expressing PA-GFP-tubulin are excited with the 488nm argon laser line and are photoactivated with a 405nm laser diode. The imaging path consists of two polarization channels that are modulated with a spatial light modulator (SLM) encoding the DH-PSF phase mask (bottom right inset). The inset in the middle shows PtK1 microtubules imaged in the horizontal and vertical channels with the standard PSF (SLM off) and with the DH-PSF (SLM loaded with DH-PSF mask). M refers to mirrors; QWP is a quarter wave plate;  $L_w$  is a 75mm wide-field lens;  $L_o$  is a 1.3NA objective;  $L_t$  is a 150mm achromatic lens;  $L_{s1}$ ,  $L_{s2}$ , and  $L_{s3}$  are 250mm achromatic lenses; PBS is a broadband polarization beam splitter; HWP is a broadband half wave plate; EMCCD is an electron multiplying charge coupled device detector.

In the microscope section, a 1.3NA objective ( $L_o$ ) and an achromatic lens ( $L_t$ ) form a 91X magnified intermediate image of the sample. A diaphragm (iris) is placed in this plane to adjust the field of view of the system. The polarization-sensitive signal processing section consists of two parallel 4f imaging systems - one for each of the horizontal and vertical polarizations. A broadband polarization beam splitter (PBS) creates the two polarization channels after propagation through the Fourier transform lens  $L_{s1}$ . A spatial light modulator (SLM) is placed in the Fourier plane shared by the two polarization channels. Because the SLM is sensitive only to vertically polarized light, a broadband half-wave plate is used to rotate the polarization of the horizontal channel by 90°. The two channels are engineered to exhibit the DH-PSF by loading the SLM with the DH-PSF phase mask (bottom right inset in Fig. 1). Note that the two channels are asymmetric with respect to the SLM to avoid the back-propagation of the horizontal channel beam path along the vertical channel and vice versa. Specifically, the incident angles with respect to the normal to the SLM plane are 43° and 30°, for the horizontal and the vertical channels respectively. Each of two channels is calibrated

separately to account for this asymmetry. The final stage of the 4f systems is implemented by two achromatic lenses ( $L_{S2}$  and  $L_{S3}$ ) that create two polarization-specific DH-PSF images on different regions of an electron multiplying charge coupled device (EMCCD) detector.

The illumination side of the system consists of a circularly polarized 488nm Argon laser beam (for the excitation of PA-GFP molecules) and a circularly polarized 405nm laser diode beam (for the photoactivation of PA-GFP molecules), expanded sufficiently by a wide-field lens ( $L_W$ ) to illuminate the entire field of view (40 $\mu$ m diameter) of the system. While the Dichroic<sub>1</sub> transmits over 95% of the 488nm beam and reflects over 90% of the 405nm beam, the Dichroic<sub>2</sub> and a band-pass filter in the imaging path block the excitation/activation wavelengths and transmit about 90% of the PA-GFP emission spectrum (505nm to 590nm).

The center inset in Fig. 1 shows the result of imaging PA-GFP labeled microtubules of a fixed PtK1 cell using standard PSF (SLM off) and DH-PSF (SLM loaded with DH-PSF mask), with horizontal and vertical polarization channel images in each case. In the standard PSF image, the microtubules near the focal region of the objective appear clear (because the standard PSF is narrow in this region), and the microtubules outside the focal region appear blurred (because the standard PSF widens significantly for out-of-focus objects). In contrast, in the DH-PSF image each axial (z) slice of the object is convolved with the two DH-PSF lobes, which are oriented at an angle that is uniquely related to the axial position of the object slice. 3D information can be retrieved from such DH-PSF images of continuous objects using deconvolution techniques [22]. However, in the context of photoactivation-localization based superresolution imaging, because only sparse subsets of molecules are turned on at any given time, the image of each molecule directly displays two DH-PSF lobes.

### 2.1 Channel calibration

Figure 2 shows an example of imaging a 40nm wide fluorescent bead (Excitation peak: 505nm; Emission peak: 515nm) when the SLM is loaded with the DH-PSF phase mask.

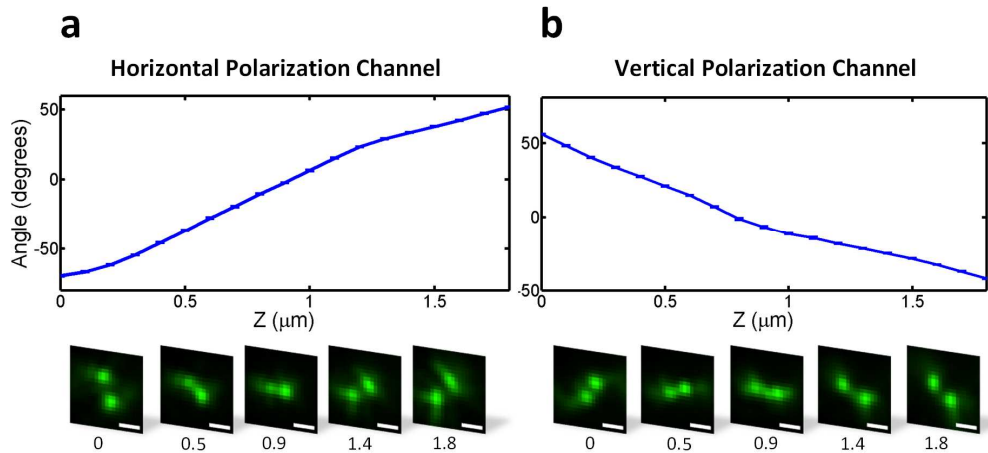


Fig. 2. Plots of DH-PSF rotation angle in the (a) horizontal and the (b) vertical channels obtained by moving a 40nm fluorescent microsphere in the axial dimension with 100nm steps. The DH-PSF rotates in opposite direction in the two channels. Scale bar: 1 $\mu$ m

Because the bead acts like a point source, the images of the bead mimic the 3D DH-PSF, with two lobes continuously rotating as the bead is moved in the axial dimension. Interestingly, because of the presence of an additional mirror between the SLM and the second signal processing lens ( $L_{S3}$ ) in the vertical channel, the two channels see horizontally flipped versions of the DH-PSF mask, resulting in opposite directions of DH-PSF rotation. However, because the total number of reflections in both channels is of the same parity, the images produced by the two channels are not flipped with respect to each other (See Fig. 1

center inset). Figure 2 shows the calibration curves for mapping rotation angles to axial locations in both polarization channels (See Appendix D for details).

When the sample under observation has multiple sparse point sources (molecules, beads) at different 3D locations, the DH-PSF images of the two channels exhibit two differently rotated lobes for every source. The transverse position of each source is estimated from the midpoint of the two lobes [13], and the axial position is estimated by converting each rotation angle to an axial location [13] using the calibration plots of Fig. 2.

### 3. Precision gain in optimal channel combination

The precision with which the 3D position of a point source can be estimated depends not only on the number of photons emitted by the source, but also on the PSF shape, detector noise, image background, and the position estimation algorithm. Because of the splitting of photons into two polarization channels, the 3D localization precision of each channel, in general, is worse than that of a single-channel system (such as a polarization insensitive superresolution system). Interestingly, precisions better than those from the individual polarization channels – even matching the precision of a single-channel system – can be achieved by properly combining the information from the two channels. From an information theoretical perspective [23], this improved precision is the result of the addition of the Fisher Information from the two channels. While such improvements can be achieved with complex estimators that simultaneously fit the PSFs of the two channels, we now show that equally improved precisions can be achieved by *optimally* combining the information with simple estimators that operate on each of the two channels separately. In a shot-noise limited system, we further show that the improved precisions achieved by this optimal combination are identical to the precisions that would have been obtained if all photons were detected in a single-channel system.

We estimate the 3D positions of the two channels separately, and combine them as a weighted average with optimal weights, as shown below.

$$P_C = \alpha P_H + \beta P_V, \quad (1)$$

where  $P_H$ ,  $P_V$ , and  $P_C$  refer to the position estimates in the horizontal channel, vertical channel, and in the channel combination along a particular spatial dimension (X, Y, or Z) with standard deviations  $\sigma_H$ ,  $\sigma_V$ , and  $\sigma_C$ , respectively.  $\alpha$  and  $\beta$  represent the scaling factors whose optimal values are given in Eq. (2) (See Appendix A for details):

$$\alpha = \frac{\sigma_V^2}{\sigma_H^2 + \sigma_V^2} ; \quad \beta = \frac{\sigma_H^2}{\sigma_H^2 + \sigma_V^2}, \quad (2)$$

Assuming uncorrelated pixels, we quantify the improvement in precision with the variable *precision gain* (PG) defined in Eq. (3).

$$PG = \min(\sigma_H, \sigma_V) - \sigma_C = \min(\sigma_H, \sigma_V) - \sqrt{\alpha^2 \sigma_H^2 + \beta^2 \sigma_V^2}. \quad (3)$$

By choosing  $\alpha$  and  $\beta$  optimally, we achieve improved precisions ( $PG > 0$ ) for all values of  $\sigma_H$  and  $\sigma_V$  (Fig. 3a) with improvements up to about 30%. It is worth noting that suboptimal selection of weights would result in precision improvements only within smaller regions of Fig. 3a. Interestingly, in a shot-noise limited system, the precision improvement with optimal weights makes the precision ( $\sigma_C$ ) of the optimally combined estimate ( $P_C$ ) identical to the precision ( $\sigma_s$ ) of a single-channel system, where all photons from a molecule are imaged in one channel (See Appendix B for details). Specifically, this result is expressed in Eq. (4).

$$\sigma_C = \sigma_s = \frac{\sigma_H \sigma_V}{\sqrt{\sigma_H^2 + \sigma_V^2}}. \quad (4)$$

Further, when  $\sigma_H^2$  and  $\sigma_V^2$  reach the Cramer-Rao Bounds (lowest possible variances with unbiased estimators) of the two channels,  $\sigma_C$  is exactly equal to the precision obtained when the Fisher Information from the two channels are added (See Appendix C for details).

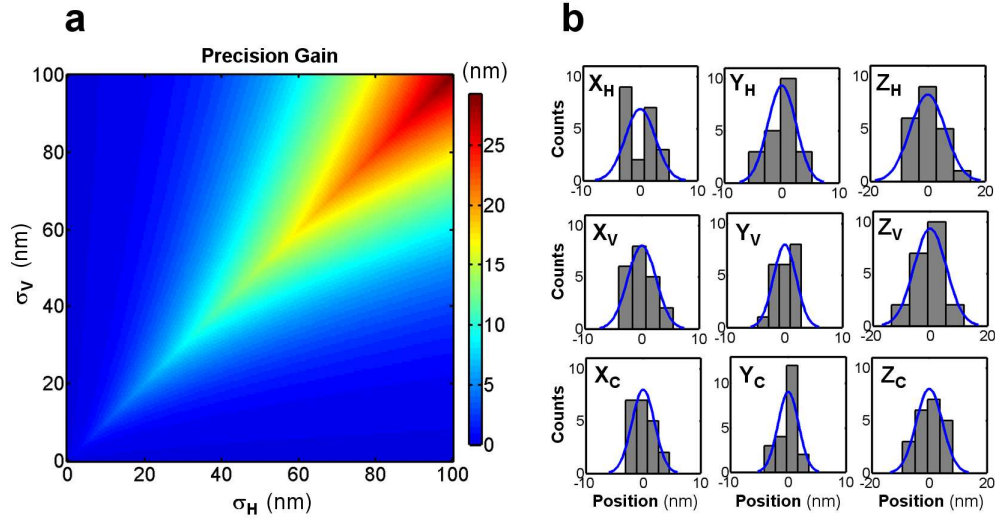


Fig. 3. (a) Gain in position localization precision obtained by optimally combining position information from the two polarization channels. (b) 3D position histograms of a fluorescent bead showing improved precisions when the horizontal ( $X_H$ ,  $Y_H$ ,  $Z_H$ ) and the vertical ( $X_V$ ,  $Y_V$ ,  $Z_V$ ) channel estimates are combined ( $X_C$ ,  $Y_C$ ,  $Z_C$ ).  $\sigma_H(X, Y, Z) = (2.6, 2.5, 6.1)nm$ ;  $\sigma_V(X, Y, Z) = (2.5, 2.5, 5.6)nm$ ;  $\sigma_C(X, Y, Z) = (2, 1.8, 4.5)nm$ .

Figure 3b shows position localization histograms obtained from 21 position estimates of a fluorescent bead. ( $X_H$ ,  $Y_H$ ,  $Z_H$ ), ( $X_V$ ,  $Y_V$ ,  $Z_V$ ), and ( $X_C$ ,  $Y_C$ ,  $Z_C$ ) correspond to the 3D position estimates obtained from the horizontal channel, the vertical channel, and the channel combination, respectively. While the single-image standard deviations of the horizontal and the vertical channels are  $\sigma_H(X, Y, Z) = (2.6nm, 2.5nm, 6.1nm)$  and  $\sigma_V(X, Y, Z) = (2.5nm, 2.5nm, 5.6nm)$ , the standard deviations of the optimal channel combination are  $\sigma_C(X, Y, Z) = (2nm, 1.8nm, 4.5nm)$ . In this experiment, 41014 photons were detected per estimate from the horizontal channel, and 65852 photons were detected per estimate from the vertical channel, after background correction in each case. The channel combination results demonstrate an improvement in precision over the precisions of the individual channels.

As a corollary, it is worth noting that  $\sigma_H$  and  $\sigma_V$  can be directly translated into information about molecule polarization orientations. However, while using high NA objectives, care needs to be taken to account for polarization distortion effects, which require rigorous vectorial electromagnetic modeling and correction of the raw polarization channels result [15].

#### 4. Polarization sensitive 3D superresolution imaging of PA-GFP molecules in a PtK1 cell

We now describe polarization sensitive 3D superresolution imaging of PtK1 (Rat Kangaroo Kidney Epithelial) cells expressing PA-GFP-tubulin. The PA-GFP molecules are excited with the 488nm laser and reactivated with the 405nm laser. Figure 4 shows an example of a PA-GFP molecule obtained from the horizontal channel of our system. The molecule position was localized from 19 images to obtain the 3D position histograms shown in Fig. 4b-d. On an average, these position estimates were computed from only 246 detected photons per image



(after background correction), resulting in single image standard deviations of  $\sigma_{PA-GFP}(X,Y,Z) = (13.2nm, 20.3nm, 42.8nm)$ .

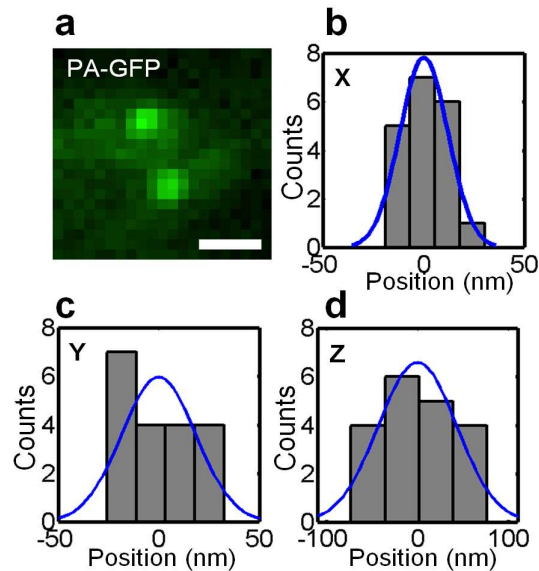


Fig. 4. Position localization histograms of a (a) single PA-GFP molecule in the (b) X, (c) Y, and (d) Z dimensions.  $\sigma_{PA-GFP}(X,Y,Z) = (13.2nm, 20.3nm, 42.8nm)$ . The average number of detected photons per image is only 246 photons. Scale bar: 1 μm

For superresolution imaging, we initially bleached the PA-GFP molecules within the field of view using the 488nm laser, then activated sparse subsets of PA-GFP molecules by shining the 405nm laser on the sample. These photoactivated molecules were subsequently excited with the 488nm laser and their emissions were recorded for 500ms (See Appendix E for details). By repeating this activation cycle, different sparse PA-GFP molecules were photoactivated, while their 3D positions were estimated from the horizontal and the vertical channels of the system. The 3D superresolution images in Fig. 5 were obtained by finding the positions of molecules from a number of activation cycles after correcting for stage drift and other systematic errors (See Appendix D).

The PtK1 cells appear differently in the horizontal and the vertical polarization channel images. For example, the edge of the cell (indicated by dotted cyan arrows) is more prominent in the horizontal polarization channel than in the vertical polarization channel (See XY projection images). This difference is due to molecules showing up with different intensities in the two channels based on their orientations. The XZ and YZ projections of the 3D superresolution images also show this polarization-based difference. These axial images also show the existence of intracellular layers extending in depth. Such polarization-specific 3D superresolution images of cells offer biologists a new way to analyze intracellular structure and function.

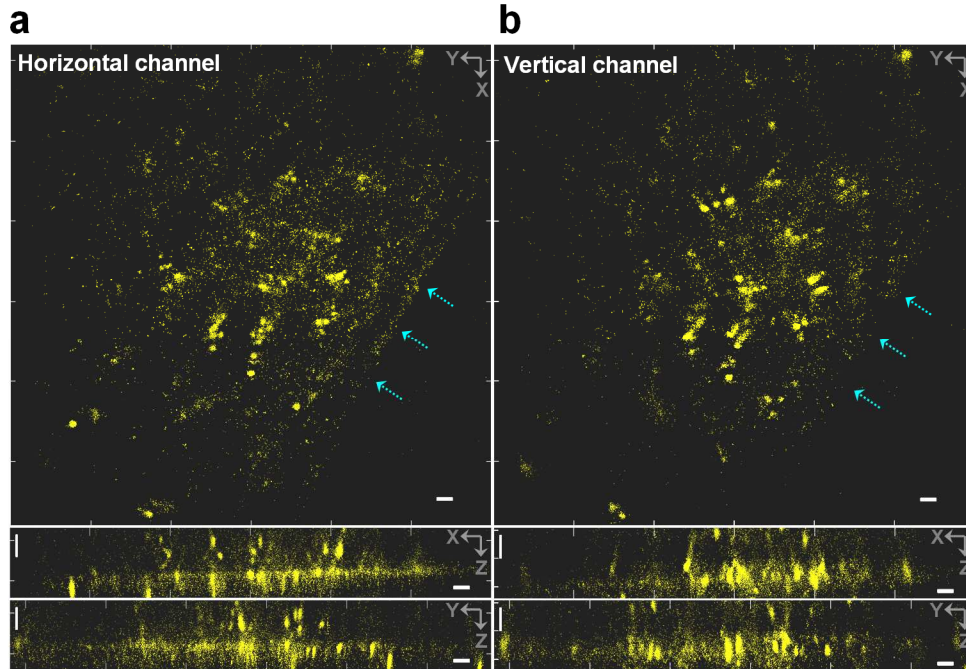


Fig. 5. Polarization specific 3D superresolution images of a PtK1 cell obtained from (a) horizontal and (b) vertical polarization channels. The superresolution images from the two channels reveal polarization specific features of the cell. For example, the edge of the cell (indicated by cyan dotted arrows) is more prominent in the horizontal than the vertical polarization channel. Scale bars: 1  $\mu\text{m}$

Standard bright field microscopy analysis of the sample using cross-polarizers showed essentially no sample birefringence (See Appendix F). Accordingly, the polarization information provided by the system can be associated with the molecular orientation and propagation through the optical system.

## 5. Discussion

In photoactivation-localization techniques, the factors contributing to contrast are the density of molecule position estimates and the number of photons detected for each position estimate. An attractive aspect of the technique presented here is the existence of an additional contrast mechanism based on polarization. In other words, polarization information can reveal structural and functional properties that might go undetected in polarization insensitive techniques.

A liquid-crystal, SLM-based implementation of the DH-PSF offers the convenience of rapidly implementing different DH-PSF masks suitable for application-specific requirements with high sampling rates and fill factors, but it unfortunately requires the absorption of the polarization component orthogonal to the polarization component for which the SLM is designed to operate. The polarization-sensitive DH-PSF method described here, on the other hand, takes advantage of photons emitted in both polarization states to improve localization precision and consequently imaging resolution, while simultaneously having the ability to resolve polarization specific nanometer scale features in three dimensions.

It is worth emphasizing that the objective of this work was not to measure the 3D orientation of single molecule dipoles, but to introduce a polarization based contrast in 3D superresolution imaging. Note that the polarization specific DH-PSF superresolution system in Fig. 1 detects only the first two ( $S_0$ ,  $S_1$ ) of the four Stokes parameters [24] ( $S_0$ ,  $S_1$ ,  $S_2$ ,  $S_3$ ) corresponding to an arbitrary transverse-plane polarization state. In order to determine the transverse-plane orientation of an arbitrary linear polarization state,  $S_2$  must be measured in



addition to  $S_0$  and  $S_1$ . This can, for example, be done by decomposing the incoming polarization into two additional  $+45^\circ$  and  $-45^\circ$  channels.

Polarization sensitive detection of single molecules using the DH-PSF provides information from both the 3D position and the orientation of individual fluorescent proteins within a cell or sub-cellular structure. Note that this polarization-sensitive information corresponds to the fluorescent protein rather than the protein it is fused to. In the case of fluorescent protein fusions, the linker domain that connects the fluorescent protein to the protein of interest may be flexible. A future challenge will be to link proteins of interest to fluorescent probes that are limited in their mobility. Future work towards full wide-field imaging of 3D orientations of single molecules should also address the determination of all the Stokes parameters taking into account the polarization modifications introduced by high NA optics, while also including well-known techniques of image registration to combine different polarization channels. The latter is facilitated by the availability of fiduciary particles.

Applications of this technique for biology are far-reaching, with use in tracking orientation changes of molecules within a cellular structure, as well as in monitoring interactions between molecules. For example, solving the orientation of proteins within large subcellular structures, such as centrosomes or kinetochores, would provide important information on how protein-protein interactions occur within these structures, and on how signals are exchanged between these structures and the cytoplasm of the cell. Further, polarization sensitive superresolution imaging of individual cytoskeletal subunits (i.e. actin, tubulin) can potentially be used to detect the binding of proteins to actin or microtubule filaments with high precision. Understanding the precise location and orientation of protein binding to these filaments would provide much needed insight into a number of critical cellular processes including chromosome segregation, cell motility, neurite outgrowth, and vesicle trafficking.

## 6. Conclusion

In conclusion, we demonstrated a polarization sensitive 3D superresolution imaging system that engineers the PSFs of two orthogonal polarization channels with a single SLM and detects both channels separately with a single detector. By combining the position information from the two imaging channels with simple estimators, we demonstrated significant improvements in 3D localization precision. The system was used to obtain polarization specific 3D superresolution images of PtK1 cells expressing PA-GFP.

## Appendix A: Derivation of optimal weights for weighted channel combination

Assuming uncorrelated pixels, the standard deviation of the weighted average channel combination defined in Eq. (1) of main text is,

$$\sigma_c = \sqrt{\alpha^2 \sigma_H^2 + (1-\alpha)^2 \sigma_V^2}, \quad (5)$$

where the weight condition,  $\alpha + \beta = 1$ , has been used to express  $\beta$  in terms of  $\alpha$ . Optimal weights are defined as the weights that minimize  $\sigma_c$ . Applying the minimization condition by equating the first derivative (with respect to  $\alpha$ ) of Eq. (5) to 0,

$$\frac{\partial \sigma_c}{\partial \alpha} = \frac{2\alpha \sigma_H^2 - 2(1-\alpha) \sigma_V^2}{2\sqrt{\alpha^2 \sigma_H^2 + (1-\alpha)^2 \sigma_V^2}} = 0. \quad (6)$$

Solving Eq. (6) for  $\alpha$  leads to

$$\alpha = \frac{\sigma_V^2}{\sigma_H^2 + \sigma_V^2}; \quad \beta = \frac{\sigma_H^2}{\sigma_H^2 + \sigma_V^2}. \quad (7)$$

The second derivative (with respect to  $\alpha$ ) of Eq. (5) is positive, confirming that  $\sigma_C$  attains its minima when the weights are as defined in Eq. (7). Using (7) in (5), the standard deviation of the channel combination becomes,

$$\sigma_C = \frac{\sigma_H \sigma_V}{\sqrt{\sigma_H^2 + \sigma_V^2}}. \quad (8)$$

#### Appendix B: Equality of the precision of the optimal channel combination ( $\sigma_C$ ) and the precision of single-channel systems ( $\sigma_S$ )

In a shot noise limited system, if  $N$  is the number of photons captured by an imaging system from a molecule,  $\sigma_S$  is the standard deviation if all  $N$  photons are imaged in one channel, and  $\kappa$  is the fraction of photons entering the horizontal polarization channel, the standard deviations corresponding to horizontal ( $\sigma_H$ ) and vertical ( $\sigma_V$ ) polarization channels are,

$$\sigma_H = \frac{\sigma_S}{\sqrt{\kappa}}; \quad \sigma_V = \frac{\sigma_S}{\sqrt{1-\kappa}}. \quad (9)$$

From Eq. (9),

$$\sigma_S = \sigma_V \sqrt{1-\kappa} = \sigma_V \sqrt{1 - \frac{\sigma_S^2}{\sigma_H^2}}. \quad (10)$$

Solving Eq. (10) for  $\sigma_S$ ,

$$\sigma_S = \frac{\sigma_H \sigma_V}{\sqrt{\sigma_H^2 + \sigma_V^2}}. \quad (11)$$

Note that from Eqs. (8) and (11),  $\sigma_C$  and  $\sigma_S$  are identical. This means that (in the shot-noise limited case) the precision achieved by optimally combining channels is exactly the same as the precision of a single-channel system, where all photons from a molecule are imaged in one channel.

In summary, the weighted combination method of Eq. (1) in the paper, when used with the optimal weights of Eq. (7), is found to be a powerful, yet simple, method that achieves precisions that are equivalent to the precisions of a system that detects all photons in a single channel.

#### Appendix C: Equality of the Cramer Rao Bound (CRB) of the optimal channel combination ( $CRB_C$ ) and the CRB of a two-channel ( $CRB_T$ ) system

CRB is a quantitative information theoretical metric that provides a lower bound on the estimator variance when unbiased estimations are used. We now show that the CRB of the optimal channel combination ( $CRB_C$ ) is identical to the CRB of the two channel system ( $CRB_T$ ) and also to the CRB of a single-channel system ( $CRB_S$ ) that captures all the photons.

Using Eq. (8) and taking the lower bound on both sides of the equation, we obtain the CRB corresponding to the optimal weighted average rule,

$$CRB_C = \frac{CRB_H CRB_V}{CRB_H + CRB_V}, \quad (12)$$

where  $CRB_H$ ,  $CRB_V$  are the lower bounds of the horizontal ( $\sigma_H^2$ ) and vertical ( $\sigma_V^2$ ) channel variances, respectively.

The total information content in a two channel system is given by the sum of the Fisher Information from individual channels ( $F_H \equiv 1/CRB_H$  and  $F_V \equiv 1/CRB_V$ ). Hence, the CRB for the two channel system is

$$CRB_T = \frac{1}{F_H + F_V} = \frac{CRB_H CRB_V}{CRB_H + CRB_V}. \quad (13)$$

From Eqs. (12) and (13), we see that  $CRB_C = CRB_T$ . Similarly, by applying lower bounds on Eq. (11), it follows that  $CRB_C = CRB_S$ .

The fact that  $CRB_C$  is identical to  $CRB_T$  suggests that estimators acting separately on each of the two channels can be as good as the (more complex) estimators that operate simultaneously on the two channels.

#### Appendix D: Rotation angle calibration and transverse position corrections

The data for the plots in Fig. 2 of main text were obtained by translating a 40nm wide fluorescent microsphere (Invitrogen yellow-green carboxylate-modified FluoSpheres®) in 100nm axial steps using a piezo stage (Physik Instrumente P-615.3CD), and by estimating the DH-PSF rotation angle from 21 images acquired with 273ms exposure time with a detector cooled to  $-90^\circ\text{C}$ . These fluorescent microspheres have an emission spectrum that is very close to that of PA-GFP. The 488nm excitation power was 1.3mW. DH-PSF rotation angles were estimated as the angle between the centroids of the two DH-PSF lobes. The standard deviation of the angle estimator at each axial step is shown as an error bar in Fig. 2.

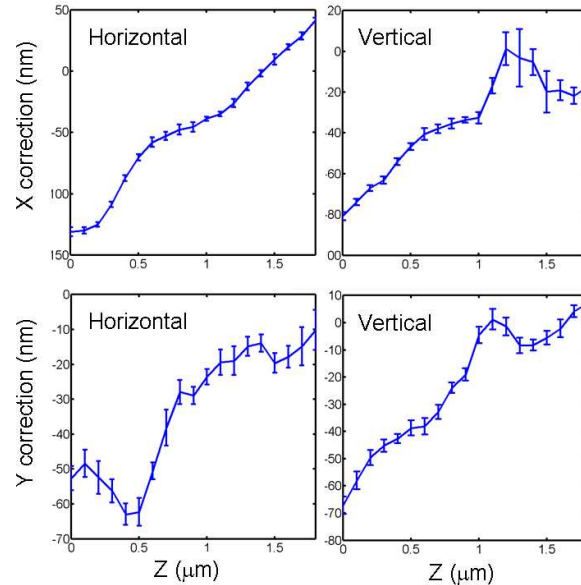


Fig. 6. X and Y corrections of horizontal and the vertical channels due to aberration-induced systematic shifts in the midpoint of the two PSF lobes.

Because of aberrations, the position of the midpoint of the two DH-PSF lobes shifts with axial distance. This systematic shift is calibrated by plotting the transverse position of the midpoint as a function of axial distance (Fig. 6). This correction exhibits transverse spatial invariance, as verified experimentally with different beads distributed across the field of view. Actual 3D position information of a point source is reported after correcting for these systematic errors.

## Appendix E: Superresolution imaging – experimental details

The 405nm diode laser (0.5mW power) was controlled with a function generator to turn on for 500ms once every 5 seconds. The 488nm Argon laser (38mW power) was always on during the imaging process. The laser beams illuminated the sample with circular polarization to excite/photoactivate molecules with all transverse orientations. Broadband (420-680nm; Edmund Optics) polarizing beam splitter and an achromatic (465-610nm; Edmund Optics) half wave plate were used in the imaging path to account for the PA-GFP emission bandwidth. Images were detected with 500ms exposure time using an electron multiplying charge coupled device (EMCCD) detector (Andor iXon) cooled to  $-90^{\circ}\text{C}$ . In our experiment, the stage drifted over a range of 310nm (X), 320nm (Y), and 90nm (Z) during the imaging time of 3.7 hours. This drift was corrected with a fiduciary, before obtaining the polarization sensitive PALM results of Fig. 5. Some of the fiduciary objects used are Invitrogen yellow-green fluorescent microspheres (with emission spectra almost identical to that of PA-GFP), and bright spot-like regions of the cell that fluoresced throughout the imaging process. The drift correction was carried out by subtracting the displacement of the fiduciary (in each frame) from the position of every single molecule emitter in that frame.

## Appendix F: Sample preparation

PtK1 cells stably expressing PA-GFP-tubulin were maintained in HAM's F-12 medium complemented with 0.5 mg/ml G418, 10% fetal bovine serum, penicillin, streptomycin, and amphotericin B (antimycotic) and plated on number 1½, 22mm<sup>2</sup> glass coverslips in 6-well culture dishes in a 37°C, 5% CO<sub>2</sub> humidified incubator. Cells on coverslips were lysed in 0.5% Triton X-100 in PHEM buffer (60 mM PIPES, 25 mM HEPES, 10 mM EGTA, and 4 mM MgSO<sub>4</sub>, pH 6.9) at 37°C for 5 min and fixed in freshly prepared 4% formaldehyde in PHEM buffer at 37°C for 20 min. Coverslips were rinsed three times for 5 min in PHEM, mounted onto slides, and sealed.

Bright-field imaging of PtK1 cells [Differential Interference Contrast (DIC) image in Fig. 7 (a)] with cross-polarizers essentially showed no birefringence [Fig. 7 (b)].

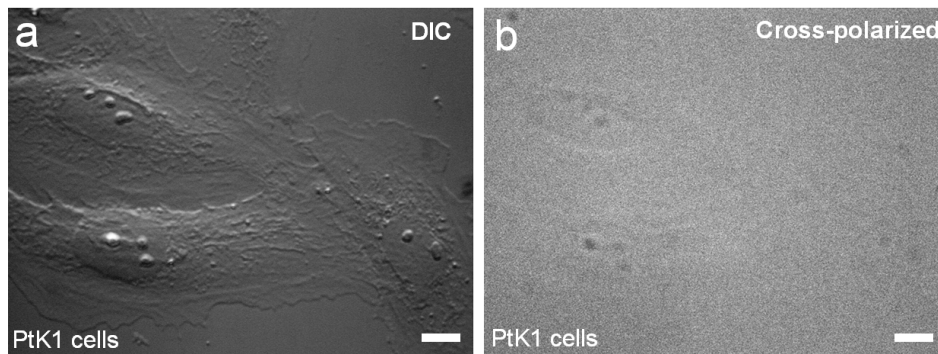


Fig. 7. (a) Differential Interference Contrast (DIC) image of PtK1 cells, (b) Cross-polarized image of the same cells as in (a) showing negligible birefringence. Scale bars: 10μm

## Acknowledgments

The authors thank J. Richard McIntosh for inspiring discussions, Alexey Khodjakov for PA-GFP-tubulin expressing cells, and Keith DeLuca for sample preparation. This work was supported by NSF awards DBI-0852885 and DGE-0801680. SRPP acknowledges support from a CDM Optics PhD Fellowship.